




Article

Temporal Changes in Mediterranean Pine Forest Biomass Using Synergy Models of ALOS PALSAR-Sentinel 1-Landsat 8 Sensors

Edward A. Velasco Pereira *, María A. Varo Martínez, Francisco J. Ruiz Gómez 
and Rafael M. Navarro-Cerrillo 

Silviculture Laboratory, Dendrochronology, and Climate Change, DendrodatLab-ERSAF, Department of Forestry Engineering, University of Cordoba, Campus de Rabanales, Crta. IV, km. 396, E-14071 Córdoba, Spain

* Correspondence: z02vepee@uco.es

Abstract: Currently, climate change requires the quantification of carbon stored in forest biomass. Synthetic aperture radar (SAR) data offers a significant advantage over other remote detection measurement methods in providing structural and biomass-related information about ecosystems. This study aimed to develop non-parametric Random Forest regression models to assess the changes in the aboveground forest biomass (AGB), basal area (G), and tree density (N) of Mediterranean pine forests by integrating ALOS-PALSAR, Sentinel 1, and Landsat 8 data. Variables selected from the Random Forest models were related to NDVI and optical textural variables. For 2015, the biomass models with the highest performance integrated ALS-ALOS2-Sentinel 1-Landsat 8 data ($R^2 = 0.59$) by following the model using ALS data ($R^2 = 0.56$), and ALOS2-Sentinel 1-Landsat 8 ($R^2 = 0.50$). The validation set showed that R^2 values vary from 0.55 (ALOS2-Sentinel 1-Landsat 8) to 0.60 (ALS-ALOS2-Sentinel 1-Landsat 8 model) with RMSE below 20 Mg ha^{-1} . It is noteworthy that the individual Sentinel 1 ($R^2 = 0.49$). and Landsat 8 ($R^2 = 0.47$) models yielded equivalent results. For 2020, the AGB model ALOS2-Sentinel 1-Landsat 8 had a performance of $R^2 = 0.55$ (validation $R^2 = 0.70$) and a RMSE of 9.93 Mg ha^{-1} . For the 2015 forest structural variables, Random Forest models, including ALOS PAL-SAR 2-Sentinel 1 Landsat 8 explained between 30% and 55% of the total variance, and for the 2020 models, they explained between 25% and 55%. Maps of the forests' structural variables were generated for 2015 and 2020 to assess the changes during this period using the ALOS PALSAR 2-Sentinel 1-Landsat 8 model. Aboveground biomass (AGB), diameter at breast height (dbh), and dominant height (Ho) maps were consistent throughout the entire study area. However, the Random Forest models underestimated higher biomass levels ($>100 \text{ Mg ha}^{-1}$) and overestimated moderate biomass levels ($30\text{--}45 \text{ Mg ha}^{-1}$). The AGB change map showed values ranging from gains of 43.3 Mg ha^{-1} to losses of -68.8 Mg ha^{-1} during the study period. The integration of open-access satellite optical and SAR data can significantly enhance AGB estimates to achieve consistent and long-term monitoring of forest carbon dynamics.

Keywords: biomass; ALOS; SENTINEL 1; LANDSAT 8; polarization; backscatter; textures; Mediterranean pine plantations



Citation: Velasco Pereira, E.A.; Varo Martínez, M.A.; Ruiz Gómez, F.J.; Navarro-Cerrillo, R.M. Temporal Changes in Mediterranean Pine Forest Biomass Using Synergy Models of ALOS PALSAR-Sentinel 1-Landsat 8 Sensors. *Remote Sens.* **2023**, *15*, 3430. <https://doi.org/10.3390/rs15133430>

Academic Editor: Nikolay Strigul

Received: 19 May 2023

Revised: 2 July 2023

Accepted: 4 July 2023

Published: 6 July 2023



Copyright: © 2023 by the authors. Licensee MDPI, Basel, Switzerland. This article is an open access article distributed under the terms and conditions of the Creative Commons Attribution (CC BY) license (<https://creativecommons.org/licenses/by/4.0/>).

1. Introduction

The management of pine plantations in Mediterranean mountain areas requires recurrent estimations and high-resolution spatial mapping of forest metrics. For foresters, tree height, diameter at breast height, basal area, and aboveground biomass (AGB) are essential parameters for planning thinning and determining the current or potential commercial value of forest stands [1]. Climate change is expected to impact natural and planted forests, becoming more vulnerable to the stress induced by biotic and abiotic factors [2,3]. These effects can be evaluated by an accurate and rapid assessment of forest biomass [4]. Most countries in the Mediterranean region conduct national forest inventories, which produce

normalized and actualized data that provide useful information, such as the distributions of the main tree species and growth changes [5,6]. However, temporal changes in forests for the purpose of spatially continuous mapping of large areas cannot be achieved using this method. Several strategies have been utilized to circumvent these surveys' limitations, such as utilizing previously collected data through statistical analysis or machine learning methods that significantly enrich disparate data sources (multi-source approaches), or integration of airborne and spaceborne remote sensing instruments (such as national low-density LiDAR) [7].

Accurate measurement of the forest biomass in terrestrial carbon accounting is necessary in the context of climate change [8–10]. Traditional field methods are time-consuming, expensive, difficult to execute, and only applicable to small areas. Additionally, accurate biomass estimations at operational scales to quantify carbon sources and sinks at regional scales are limited by the environmental, topographic, and biophysical characteristics of forest ecosystems' spatial and temporal variation [11]. Thus, remote sensing techniques are perceived to be the best alternative for improving forest biomass estimation over large areas [12]. The early studies attempting to estimate biomass using satellite remote sensing variables utilized Landsat TM data with 30 m resolution [13–15] in structurally simple temperate and boreal forests. Vegetation indexes were the most frequently employed approach in optical remote sensing for biomass estimation [16]. Most indices rely on the connection between red and near-infrared wavelengths to maximize the spectral input from green vegetation while minimizing contributions from the soil, sun angle, sensor view angle, shaded vegetation, and atmosphere [17]. However, in many forests with high biomass levels, such as closed forest canopies with several layers (e.g., tree canopy, shrubs, herbaceous) and mixed species, the vegetation indices showed poor success with their biomass estimations [18,19].

More recently, many studies have integrated optical remote sensing data with synthetic aperture radar (SAR) [9,20], airborne laser scanning (ALS) [19], and multispectral sensors for mapping forest metrics [21]. SAR imagines have demonstrated the ability to distinguish between several characteristics of forest stand structure, such as age, density, and leaf area index [21]. Improvements in SAR images have also allowed for the development of numerous texture measures based on the grey-level co-occurrence matrix and texture feature spectrum [22], which have been used as an accurate alternative to characterize areas with high values of biomass [21,23]. These promising results for biomass quantification, integrating passive-optical sensors and SAR data using texture measurement, are limited by the complexity of texture data, which can vary greatly depending on forest cover, tree cover structural elements, physiographic conditions, plant phenology, and texture processing data management [24].

Open access to SAR data and open-source image processing software presents an opportunity to develop a cost-effective method for mapping temporal changes to forest structure parameters. SAR sensors penetrate the forest canopy and are weather-independent, providing information regarding the vertical vegetation structure, such as the canopy height [25]. For instance, forest structure variables can be predicted using time series from SAR Sentinel-1C-band satellite data and derived metrics such as backscatter, slope, correlation coefficients, and texture metrics [26]. However, C-band does not penetrate the canopy very deeply [27], which reduces the precision of forest structure maps in areas of dense vegetation [28]. Consequently, a combination of SAR and optical imagery can be used to produce precise forest structure maps covering large areas [29]. Particularly, the data provided for SAR sensors (e.g., ALOS2-PALSAR, Sentinel-1) and multispectral sensors (e.g., Sentinel-2, Landsat) improve the accuracy of forest attribute predictions (e.g., tree density, height, and basal area) [30,31] and aboveground biomass [32]. However, it is unclear as to whether data from those satellite sensors can also accurately estimate temporal biomass changes.

Therefore, it is increasingly necessary to assess the integration of remote sensing data with machine learning algorithms to estimate aboveground biomass in Mediterranean pine

plantations. To achieve this goal, we compared the performances of different models using freely available satellite-derived optical, SAR, and topographic variables, contrasted with low-density ALS models and national forest inventories. The Japan Aerospace Exploration Agency (JAXA) has released freely available global mosaic data sets from ALOS PALSAR-2, one of the most widely used sensors for biomass assessment to date, with a resolution of 25 m, which can provide excellent textural information. In addition, the European Space Agency’s Copernicus Sentinel 1 mission has supplied open-access data since 2016, integrating a 10 m resolution C-band in addition to the Landsat 8 optical sensor collections available in the GEE repository. In this context, our research aimed to develop a general approach to periodically updating maps of forest structure parameters and aboveground biomass using open-source data and software. We used ALOS-PALSAR, Sentinel-1, and Landsat 8 data, as well as free software such as R, RStudio, and Google Earth Engine (GEE). The specific objectives were: (i) to select image processing methods such as spectral reflectance, simple band ratio, selected vegetation indicators, and texture processing to build a comparative model; (ii) to apply machine learning algorithms to estimate height, density, basal area, and biomass; and (iii) to elaborate maps of biomass change between two low-density national LiDAR programs (2014–2021) in areas of Mediterranean pine forest plantations. The proposed methodology can contribute to the estimation of carbon storage, adaptive silviculture, and the regulation of ecosystem services provided by Mediterranean pine plantations.

2. Materials and Methods

2.1. Study Area

The study area was located in “Sierra de Los Filabres” (Almeria province, Southeast Spain, hereafter Filabres, $37^{\circ}13'27''\text{N}$, $2^{\circ}32'54''\text{W}$, Figure 1), one of the driest regions in Western Europe (Figure S1 Supplementary Material). The climate is Mediterranean semi-arid, with an annual average rainfall of around 300 mm and an annual average temperature of 11°C , reaching a maximum temperature of 32°C in July and a minimum of -8°C in January [33]. Climate data were obtained from the meteorological station of “Calar Alto” ($37^{\circ}13'25''\text{N}$, $2^{\circ}32'46''\text{W}$), located at 2168 m.a.s.l. (http://www.caha.es/weatherng_es.html, accessed on 21 July 2022). The vegetation consisted of a 50–60-year-old *Pinus* spp. plantation, with the areas covered by *Pinus sylvestris* L. and *Pinus nigra* Arnold being noteworthy, with a current density between 509 and 1405 trees ha^{-1} . The basal area ranged from 18.33 to 40.85 $\text{m}^2 \text{ha}^{-1}$ (Table 1) [34]. The topography of Filabres is characterized by steep slopes (>35%) and a metamorphic geological formation, with a foundation of Precambrian and Paleozoic schists and quartzites.

Table 1. Silvicultural variables of *Pinus* spp. in Sierra de los Filabres (Southern Spain). Number of plots (n), diameter at breast height (dbh, cm), density (N, trees ha^{-1}), basal area (G, $\text{m}^2 \text{ha}^{-1}$), dominant height (Ho, m) and aboveground biomass (AGB, Mg ha^{-1}).

Species	n. Plots	dbh	N	G	Ho	AGB
<i>Pinus halepensis</i>	630	17.282	419.316	10.192	9.076	19.931
<i>Pinus nigra</i>	634	18.327	722.287	18.988	9.350	47.237
<i>Pinus pinaster</i>	718	23.387	534.441	23.790	11.281	42.986
<i>Pinus sylvestris</i>	104	17.774	605.043	14.410	8.743	35.235
Average	2086	19.726	560.284	17.756	9.902	36.929

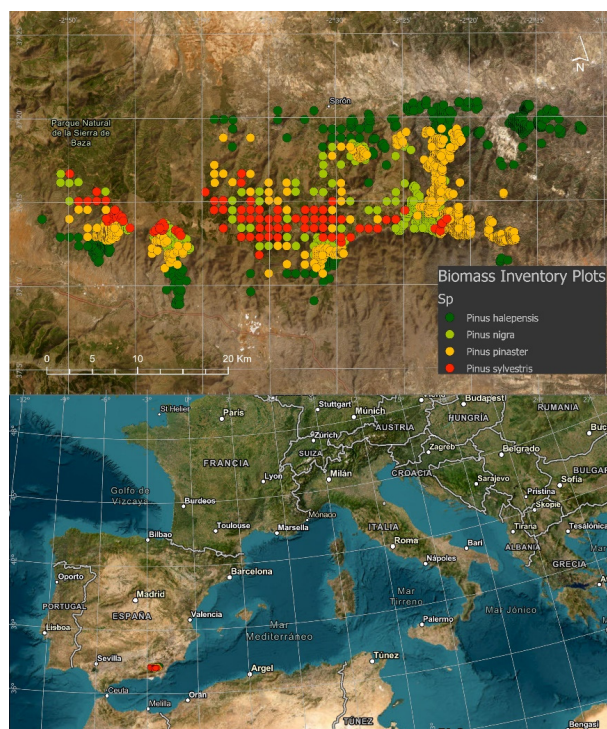


Figure 1. Study area of *Pinus* spp. plantations in Sierra de los Filabres (Southern Spain) and locations of sample plots.

2.2. Methodology Framework

Our methodology compared allometric models for field biomass estimation and ALOS PALSAR 2-Sentinel 1-Landsat-8 image date (Figure 2). As field information, the Spanish National Forest Inventory IFN3 for 2014 was used [35]. The image parameters served as independent variables, while the field plot data served as dependent variables with which simple and multivariate regression and Random Forest models could investigate the potential of various image parameters for biomass estimation.

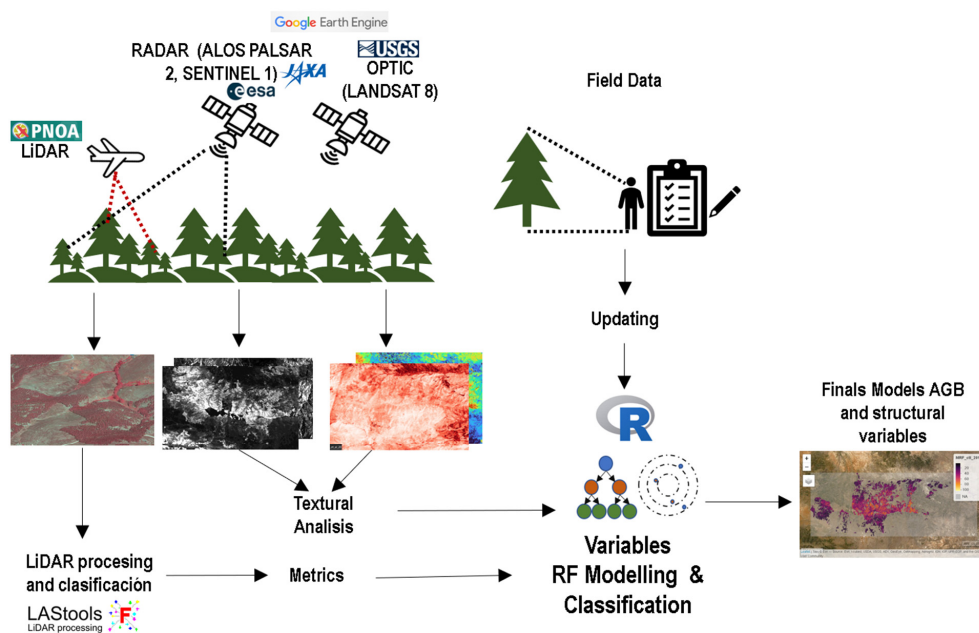


Figure 2. Flowchart for aboveground biomass estimation in Mediterranean pine plantations by integration of ALOS PALSAR 2-Sentinel 1-Landsat-8 images.

2.3. Field Plot Measurement and Field Biomass Estimation

A total of 2086 field plots were selected from stratified sampling of both the Spanish National Forest Inventory [35] and public forest management plans. As the inventory plots were measured in 2007, an updating process with the first multitemporal ALS data in 2014 (see above) was conducted following the allometric models developed in Guzmán Alvarez et al. [36], similarly to Navarrete-Poyatos et al. [34] in the same study area. Once finished, the biomass models built by Ruiz-Peinado et al. [37] were applied (Table S1 Supplementary Material).

2.4. Remote Sensing Data

2.4.1. ALOS Data

We used the data from the 25 m annual mosaics of open radar data from the ALOS PALSAR 2 (version 2) sensor, provided by the Japanese Aerospace Exploration Agency (JAXA). The images contain 2 types of polarization HH and HV in an L-band (23 cm). These mosaics were pre-processed for geometry distortion, topographic effects, and radiometric slope correction (Figure S2 Supplementary Material). The SAR datasets are available at (https://www.eorc.jaxa.jp/ALOS/en/dataset/fnf_e.htm, accessed on 15 June 2022). The data arrived in 16-bit digital levels (DN); the two polarizations were converted to gamma naught values in decibel units (dB) using the following equation (Equation (1)):

$$\gamma_0 = 10 \log_{10}(\text{DN}^2) - 83.0 \text{ dB} \quad (1)$$

Then, the dB values were converted to power backscatter using the following equation (Equation (2)):

$$\text{Gamma_pw} = 10^{(0.1 \times \text{Gamma_dB})} \quad (2)$$

With the Gamma_pw values, the normalized difference backscatter index NDBI was additionally calculated. This index is similar to the optical NDVI index, which indicates the greenness of the vegetation, but in this case, in addition to capturing the upper part of the vegetation in the optical index, the NDBI index can penetrate and differentiate different strata of the vegetation [15,38]. NDBI mitigates the effects of terrain illumination differences as well as atmospheric effects. Once the backscattering power was obtained, a speckle filter was applied during Google Earth Engine processing.

2.4.2. Sentinel 1 Data

Data from the Sentinel 1 mission of the European Space Agency were used, which allowed us to access data from the C-band (5.4 cm) dual-polarization synthetic aperture radar (SAR) instrument at 5.405 GHz. Sentinel 1 is presented in different modes: Stripmap (SM), interferometric Wide Swath (IW), Extra-Wide Swath (EW), and Wave (WV). The instrument has one transmitter and two receiver strings, so it has single and double polarization. The scenes had previously been corrected with the elimination of thermal noise, radiometric calibration, and terrain correction using STRM 30 or ASTER DEM, and the final values were obtained in decibels through the logarithmic scale. Sentinel Collection 1 is available in the Google Earth Engine Data Catalog (https://developers.google.com/earth-engine/datasets/catalog/COPERNICUS_S1_GRD, accessed on 18 June 2022). For this study, we filtered the Transmitter Receiver Polarization collections: vh (cross-polarized vertical transmit and horizontal receive) and vv (simple co-polarize, vertical transmit and vertical receive), instrument-Mode iw (Wide Interferometric Swath Mode) and orbitProperties_pass: ascending and descending. Then, we calculated the combined orbit for the asc-desc step. Finally, the values were converted to power backscatter. The Sentinel 1 variables were calculated for two periods, the first for the months between May and June and the second for the entire year. Rain events can occasionally cause increases in the signal regardless of the evolution of vegetation, since SAR backscatter is sensitive to humidity. To guarantee that the outcomes would be reproducible, we chose dates with no

precipitation in the previous three days. This made the dates less dependent on climatic conditions and yearly variations, and reduced the uncertainties brought on by rain.

2.4.3. Landsat Data

Landsat 8 OLI/TIRS optical sensor data were obtained from the LANDSAT/LC08/C02/T1_L2 collection of the Google Earth Engine (Collection 2 Level-2, (https://developers.google.com/earth-engine/datasets/catalog/LANDSAT_LC08_C02_T1_L2, accessed on 8 June 2022). They contained atmospherically corrected surface reflectance and land surface data, and had a resolution of ten meters. NDVI was calculated from the red (665 nm) and near-infrared (842 nm) bands during the months in which the vegetation was greenest (March to June) for the reference years (2014 and 2021). For NDVI calculation, a cloud mask was applied.

2.4.4. Texture Analysis

Additionally, grey-level co-occurrence matrices were used to calculate the textures of ALOS 2, Sentinel 1, and Landsat8 data [15,23,39]. Texture is a function calculated by the angular relationship and distance of two neighboring pixels in 4 directions, including horizontal, vertical, and diagonal. In this study, we used the texture's mean, variance, entropy, second angular momentum, dissimilarity, correlation, and homogeneity metrics in a 5×5 pixel window (Figure 3). The variables of texture were calculated with GLCM package in R [40], according to the methodology and equations of Haralick et al. [41]. Second-order textures were calculated for HH, HV, and NDBI SAR data, as well as NDVI optical data.

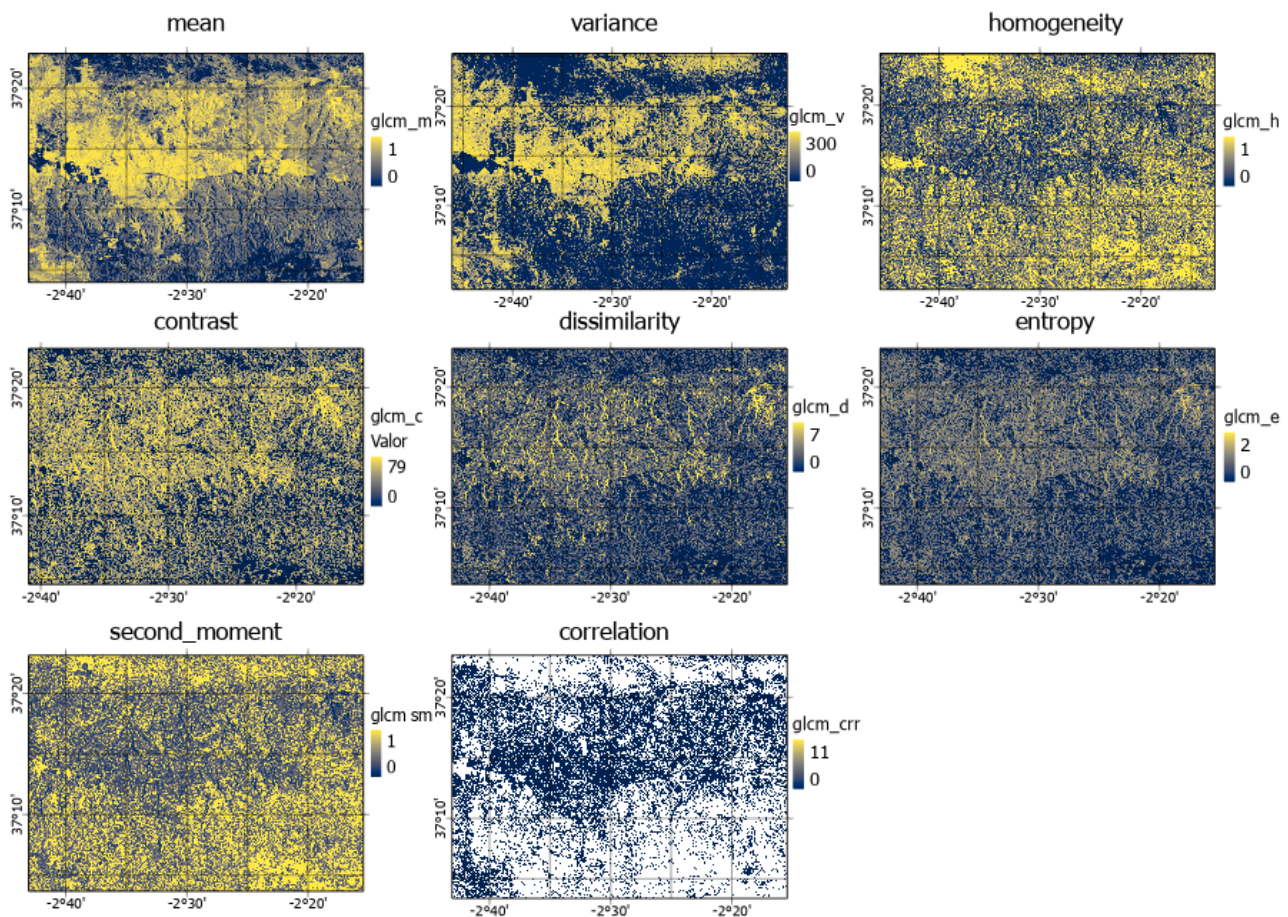


Figure 3. Textures of second order form ALOS-PALSAR 2 data in *Pinus* spp. plantations in Sierra de los Filabres (Southern Spain).

2.4.5. ALS Data Processing and Biomass Modelling

Low-density airborne laser scanning (ALS) data for the years 2014 and 2020 were provided by the PNOA (National Aerial Orthophotography Plan) through the Spanish National Geographic Information Center (<http://centrodedescargas.cnig.es/CentroDescargas/index.jsp>, accessed on 8 June 2022). The data arrived in 2 km square grids of raw points in .laz binary files in the EPSG reference system (25830 ETRS 1989/ UTM Zone 30). The ellipsoidal elevation was z , with an approximate density of 0.5 pulses m^{-2} and RMSEZ ≤ 40 cm for 2014 and a density of 2 pulses m^{-2} and RMSEZ ≤ 20 cm for 2020.

The ALS processing procedure and biomass imputation models were applied, following Navarrete-Poyatos et al. [34], to the ALS data from 2020 to assess the biomass model's accuracy by comparing it with that selected following the steps in Section 2.6 (see above). FUSION [42] and LAStools software [43] were used for LiDAR handling.

2.5. Variable Selection

An exploratory analysis of data from forest inventory plots was conducted. This included filtering outliers for model calibration, normality analysis, Pearson correlation, and variance inflation factor (VIF) for model fitting [44]. Including textural index parameters, 116 remote sensing features were extracted from the four satellite sensors (Table 2). The parameters were selected to be applied to a variety of forest types. ALOS-PALSAR-2 is more sensible for assessing woody parts of the canopy, forest height, and AGB (L-band backscatter data). We used the HV, HH, and HV/HH ratios. The C-band from Sentinel 1 was able to penetrate pine forests and was sensitive to tiny branches and leaves; thus, it could be linked to forest volume and provided information about the vegetation structure. Seven indices of texture were computed. The green leaf area, vegetation cover fraction (trees and understory), and soil properties all have an impact on spectral reflectance. Thus, photosynthetic activity and vegetation development were documented by Landsat 8 observations. It is preferable to use dates in the summer, because vegetation phenology is more stable during this season. Therefore, we used summer data for the Normalized Difference Vegetation Index (NDVI).

Table 2. Explanatory variables to estimate aboveground biomass, basal area, density, and dbh of *Pinus* spp. plantations in Southern Spain.

Data Source	Variable	Description	Season	Number of Variables
ALOS PALSAR 2	HH	Radar HH polarization	Year (2015, 2020)	1
	HV	Radar HV polarization	Year (2015, 2020)	1
	NDBI	Normalized difference backscatter index of HH and HV polarizations	Year (2015, 2020)	1
	Texture HH, HV, and NDBI	Second-order texture measures (7)	Year (2015, 2020)	21
	DEM, slope and aspect	Derived of ALOS World 3D—30 m Dem Data	-	3
Sentinel 1	vhIwAscDes	Radar vh polarization	Year—(May–June) 2015, 2020	2
	vhIwAsc		Year—(May–June) 2015, 2020	2
	vhIwDesc		Year—(May–June) 2015, 2020	2
	vvIwAscDes	Radar vv polarization	Year—(May–June) 2015, 2020	2
	vvIwAsc		Year—(May–June) 2015, 2020	2
	vvIwDesc		Year—(May–June) 2015, 2020	2
	Texture vhIwAscDes, vvIwAscDes		Year—(May–June) 2015, 2020	24
Landsat 8	reflectance	Red (SR_B4) an NIR (SR_B5) bands	Year—(May–June) 2015, 2020	6
	NDVI	Normalized difference vegetation index	Year—(May–June) 2015, 2020	2
	Texture Red, NIR and NDVI	Second order texture measures (7)	Year—(May–June) 2015, 2020	42
ALS	P90, COV AND CHM	From PNOA 2014 and 2020 (0.5 p m^{-2})	-	3
Total				116

Abbreviations: NDVI, Normalized Difference Vegetation Index; NIR, near infrared; NDBI, Normalized Difference Backscatter Index, IW, Instrument Mode Interferometric Wide Swath, Asc, Orbit Pass Ascending, Des, Orbit Pass Descending, AscDes, combined ascending and descending image collections.

2.6. Biomass and Modeling of Structural Variables

The Random Forest (RF) algorithm for machine learning was used to estimate structural forest variables. RF ranks important variables and generates an independent measure of prediction error, and has been primarily used as a classification algorithm in the remote-

sensing field. First, the variable importance was identified [45]. As suggested by Hastie et al. [46], a 5-fold cross-validation strategy was used, and the model with the lowest mean squared error was selected. Subsequently, RF models were created by combining different sensor data (optical and radar) for each of the variables: aboveground biomass (AGB), basal area (BA), number of trees per hectare (N), and diameter at breast height (dbh) (Table 1). Variables with close-to-zero variance were removed using the *nearZeroVar* tool from the *caret* package [47]. The first model was fitted with an ALOS PALSAR 2 raster data set, the second model was calibrated with a Sentinel 1 data set, the third model with Landsat 8 optical data, and the fourth with low-density ALS data. The rest of the models were combinations of variables from the information on the previous models. The data were divided into a training set and a validation set at an 80–20 ratio. For each model, a recursive elimination of variables was performed using bootstrapping techniques with the training data, employing the *rfe* function. Subsequently, models were built using the *train* function of the *caret* package. Each model was run with 10 resampling iterations and 10 cross-validation iterations using the *RepeatedCV* algorithm and the Random Forest method. With this set of variables, Random Forest models were calibrated, and the most suitable model among them was selected based on the best coefficient of determination (R^2), root mean squared error (RMSE), and the normalized RMSE (%RMSE). The coefficient of determination (R^2) is a measure of how well the model fits the data, with values closer to 1 indicating a better fit. The root mean squared error (RMSE) is a measure of the difference between the values predicted by the model and the true values. Lower RMSE values indicate a better fit. The normalized RMSE is the RMSE expressed as a percentage of the range of the true values.

The library *yaImpute* [48] in R software [49] was used for the biomass prediction according to ALS data with *k*-NN models, and the Random Forest technique was used for imputation of distances.

2.7. Biomass and Structural Variables Maps

The best models were applied to 2015 and 2020 data to estimate structural variables (i.e., density, Assman's dominant height, basal area, dbh) and biomass. The biomass change between the 2015 and 2020 period was estimated.

3. Results

3.1. Variable Selection

For the construction of the models, an exploratory analysis of all the selected variables was carried out. The strongest Pearson correlations were found for NDVI, followed by HV and HH polarizations of the ALOS PALSAR 2. (Figure S3, Supplementary Materials). From the total set of predictive variables (Table 2, reflectance, backscatter, texture, and ALS), 62 were selected by employing recursive elimination using the bootstrapping method and cross-validation (Figure S4, Supplementary Materials).

3.2. Biomass Models

3.2.1. Random Forest Variable Selection

The most important variables selected from the Random Forest models were related to NDVI (mean, variance) and optical textural variables (mean RED, Radar HV, mean HV, and HH variables) (Figure 4). Textural variables had great weight in all models, since two to four textural variables were always included among the five most important.

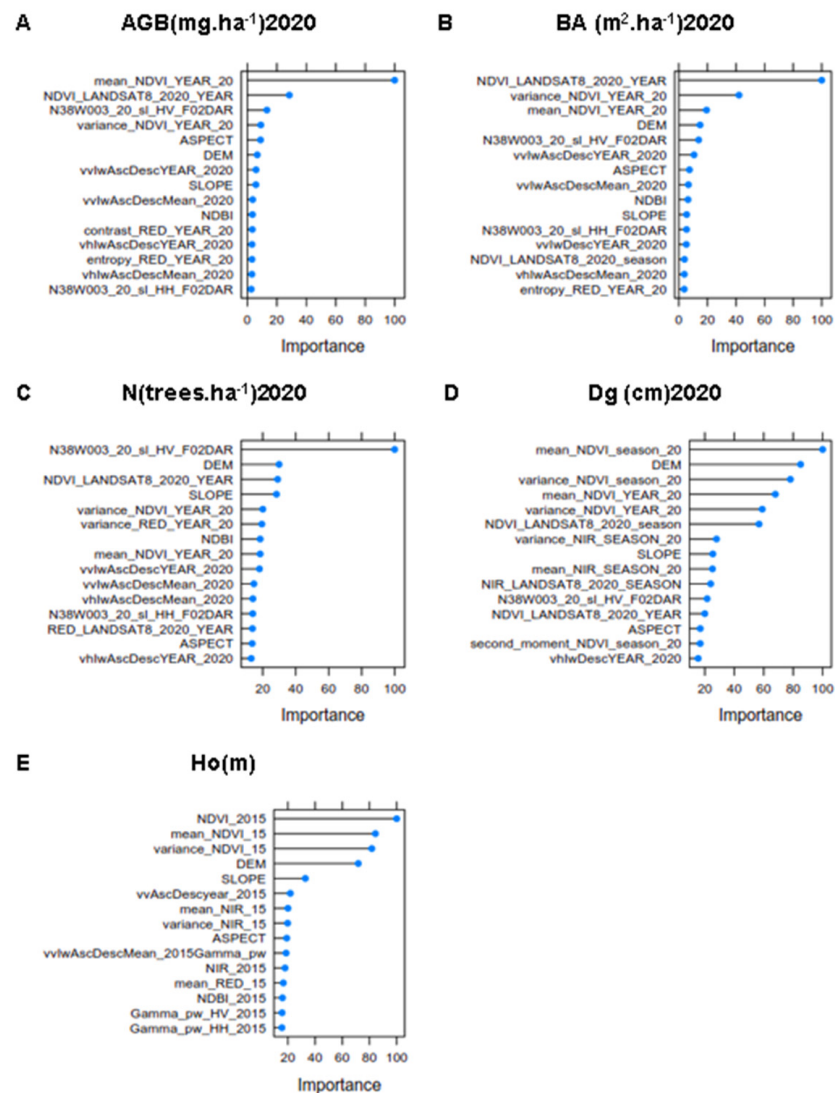


Figure 4. Variance importance ranking of predictors of the best-fitting Random Forest models for (A) aboveground biomass (AGB), (B) basal area (BA), (C) trees per hectare (N), (D) quadratic diameter (Dg), and (E) height (Ho) of *Pinus* spp. plantations in Southern Spain.

3.2.2. Random Forest AGB Models

Table 3 presents the different models used to predict the aboveground biomass (AGB) in 2015. The models with the highest performance integrated ALS-ALOS2-Sentinel 1-Landsat 8 data ($R^2 = 0.59$), followed by the models using ALS data ($R^2 = 0.56$) and ALOS2-Sentinel 1-Landsat 8 ($R^2 = 0.50$). The RMSE ranged from 21.35% to 19 Mg ha⁻¹ (Table 3). The validation set showed that the R^2 values varied from 0.55 (ALOS2-Sentinel 1-Landsat 8) to 0.60 (ALS-ALOS2-Sentinel 1-Landsat 8 model) with an RMSE below 20 mg ha⁻¹ (Table 3). It is noteworthy that the individual Sentinel 1 ($R^2 = 0.49$) and Landsat 8 ($R^2 = 0.47$) models yielded similar results. Conversely, the ALOS PALSAR 2 model performed poorly ($R^2 = 0.36$ in training and $R^2 = 0.35$ in evaluation), contrary to our expectations. Also, the combined model including ALS data did not significantly improve AGB prediction ($R^2 = 0.59$ vs. $R^2 = 0.50$ in the training data set and $R^2 = 0.6$ vs. $R^2 = 0.55$ in the evaluation data set).

Table 3. Random Forest models' performance and explanatory variables of aboveground biomass (AGB, Mg ha⁻¹, 2015) of *Pinus* spp. plantations in Southern Spain.

		AGB				
Data Set	Model	R ²	RMSE	%RMSE	BIAS	rBias (%)
Calibration	ALOS2-SENTINEL1-LANDSAT 8	0.50	21.35	57.80%	0.43	-1.41
	LIDAR-ALOS2-SENTINEL1-LANDSAT 8	0.59	19.44	53.20%	0.66	-1.24
	LIDAR	0.56	20.04	54.10%	0.86	-1.28
	LANDSAT 8_AGB	0.47	21.96	59.10%	0.47	-1.53
	ALOS2-SENTINEL1	0.49	21.54	58.30%	0.43	-1.51
	SENTINEL 1-LANDSAT 8	0.49	21.61	59.20%	0.55	-1.42
	SENTINEL 1	0.49	21.68	58.50%	0.47	-1.49
	ALOS 2	0.36	24.13	64.80%	0.50	-1.74
Validation	ALOS2-SENTINEL1-LANDSAT 8	0.55	19.88	54.50%	-0.11	-1.00
	LIDAR-ALOS2-SENTINEL1-LANDSAT 8	0.60	18.62	51.00%	-0.51	-0.62
	LIDAR	0.56	19.59	53.70%	-0.57	-0.69
	LANDSAT 8_AGB	0.52	20.54	56.30%	-0.23	-0.77
	ALOS2-SENTINEL1	0.48	21.17	58.00%	0.56	-0.94
	SENTINEL 1-LANDSAT 8	0.53	20.22	55.40%	0.14	-0.77
	SENTINEL 1	0.49	21.03	57.60%	0.55	-0.92
	ALOS 2	0.35	23.89	65.50%	-0.02	-1.25

In terms of the models' fits to observed values, models with bias values closer to zero fit the observed values better. Models with negative bias overestimated the AGB values, while models with positive bias underestimated them. Based on the bias column, we can state that the ALOS2-SENTINEL1-LANDSAT 8 model was the best fit for the observed values, both in the calibration dataset and in the validation dataset, as it had a bias value very close to zero in both sets. For 2020, we calculated the AGB model using ALOS2-SENTINEL1-LANDSAT 8, which had a performance of R² = 0.59 and an RMSE of 8.89 Mg ha⁻¹ for the training set and R² = 0.68 and an RMSE of 9.93 Mg ha⁻¹ for the testing set.

For the forest structural variables, Random Forest models, including the ALOS PAL-SAR 2-Sentinel 1 Landsat 8, variables explained between 30% and 55% of the total variance of the examined vegetation attributes expected for the 2015 models. For the 2020 model, they explained between 44% and 70% of the variance. This was higher for biomass and basal area and lower for density and dbh (Table 4). In general, the R² values for the validation dataset were better than the calibration dataset for both years. Additionally, the RMSE values were lower for 2020 than for 2015, suggesting that the model for 2020 was more accurate than the model for 2015, and the Bias values for the 2020 model were also closer to zero than the 2015 model, indicating that the 2020 model's predictions were less biased.

Table 4. Random Forest models' performance in 2015 and 2020 for the structural variables of diameter at breast height (dbh, cm), density (N, trees ha⁻¹), basal area (G, m² ha⁻¹), dominant height (Ho, m), and aboveground biomass (AGB, Mg ha⁻¹).

Data Set	Forest Structure Variable	2015 Model					2020 Model				
		ALOS2-SENTINEL1-LANDSAT 8					ALOS2-SENTINEL1-LANDSAT 8				
		R ²	RMSE	%RMSE	BIAS	rBias%	R ²	RMSE	%RMSE	BIAS	rBias%
Calibration	AGB	0.50	21.35	0.58	0.43	-1.41	0.68	9.33	0.29	0.23	-0.11
	BA	0.47	10.12	0.57	0.21	-1.29	0.50	9.78	0.56	0.18	-1.27
	N. Trees	0.31	329.97	0.58	4.71	-1.31	0.30	332.06	0.59	2.12	-1.33
	Dmc	0.34	4.60	0.24	-0.12	-0.05	0.39	4.41	0.23	-0.13	-0.04
	Ho_m	0.31	2.11	0.21	-0.01	-0.01	0.35	2.04	0.21	-0.02	-0.04
Validation	AGB	0.55	19.88	0.55	-0.11	-0.77	0.70	8.89	0.29	0.23	-0.10
	BA	0.55	9.33	0.53	0.02	-0.64	0.55	9.27	0.53	0.36	-0.60
	N. Trees	0.30	308.87	0.58	-19.49	-0.73	0.25	319.60	0.60	-21.73	-0.78
	Dmc	0.47	4.14	0.21	0.09	-0.04	0.48	4.10	0.21	0.16	-0.03
	Ho_m	0.46	1.98	0.20	0.10	-0.03	0.44	2.01	0.20	0.16	-0.02

Cross-validation between the Random Forest-predicted variables and ALS data (Figure 5) was conducted. For the N trees model, the line sloped to the left above the reference line, and the bias was negative and very high, indicating that the values were strongly over-fitted. For the other models, the line sloped to the right of the reference line, indicating that the models were slightly under-fitted, as the bias was negative and close to 0.

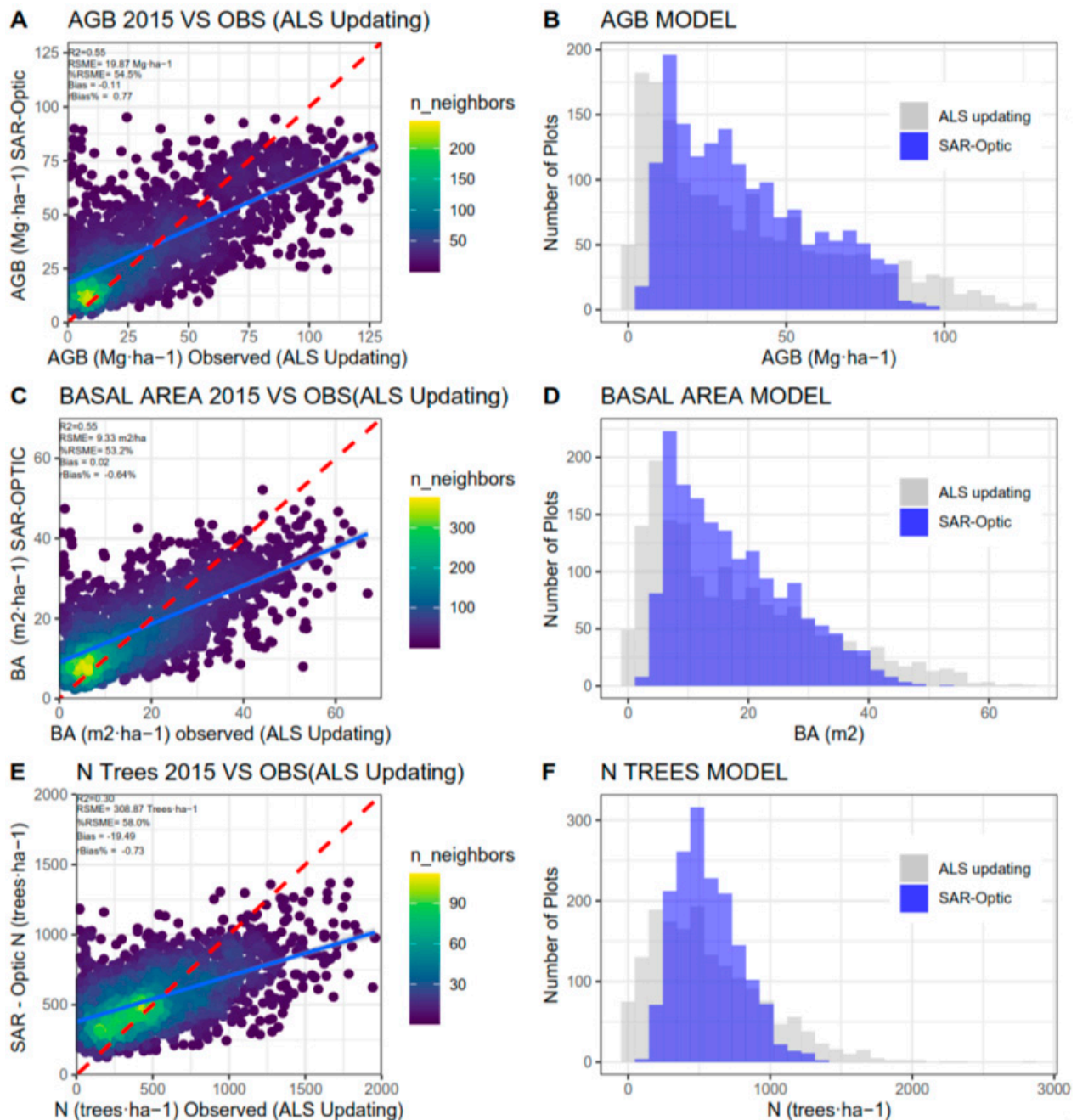


Figure 5. Cont.

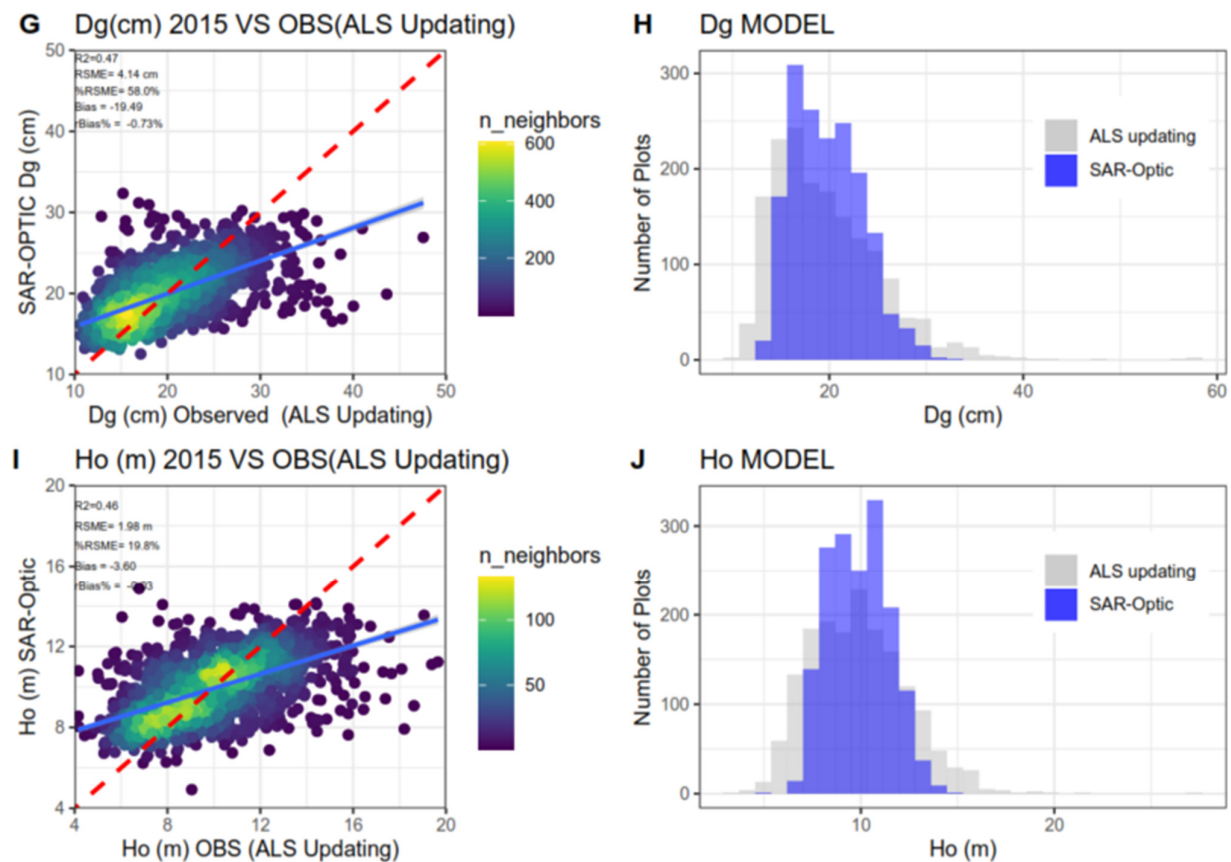


Figure 5. Scatterplots for the regression model of forest structural attributes: (A) aboveground biomass (AGB), (C) basal area, (E) density (N), (G) diameter at breast height (Dg), and (I) Assman's dominant height; 1:1 line in solid black and fitted line in dashes. R = coefficient of determination; RMSE = root mean square error and bias of the final models (ALOS PALSAR 2-SENTINEL1-LANDSAT8); the red line shows the 1:1 line references, the blue line shows the Random Forest regression model. Associated histograms (B,D,F,H,J) are shown on the right of plots between the ALS and SAR optic models.

3.3. Biomass Maps and Temporal Change

Maps of forest structural variables were generated for 2015 and 2020 to assess changes during this period (Figures 6 and 7, Figures S7–S15, Supplementary Material) using the ALOS PALSAR 2-Sentinel 1-Landsat 8 model and the second-order textures derived from both data sets. The presented AGB, Ho, dbh, density, and dominant height maps were consistent throughout the entire study. However, the RF model underestimated higher biomass levels ($>100 \text{ Mg ha}^{-1}$) and overestimated moderate biomass levels ($30\text{--}45 \text{ Mg ha}^{-1}$), as shown by the histograms for the 2015 models in Figure 5 (those for 2020 are shown in Figure S6, Supplementary Materials).

The AGB change map showed values ranging from gains of 43.3 Mg ha^{-1} to losses of 68.8 Mg ha^{-1} during the study period.

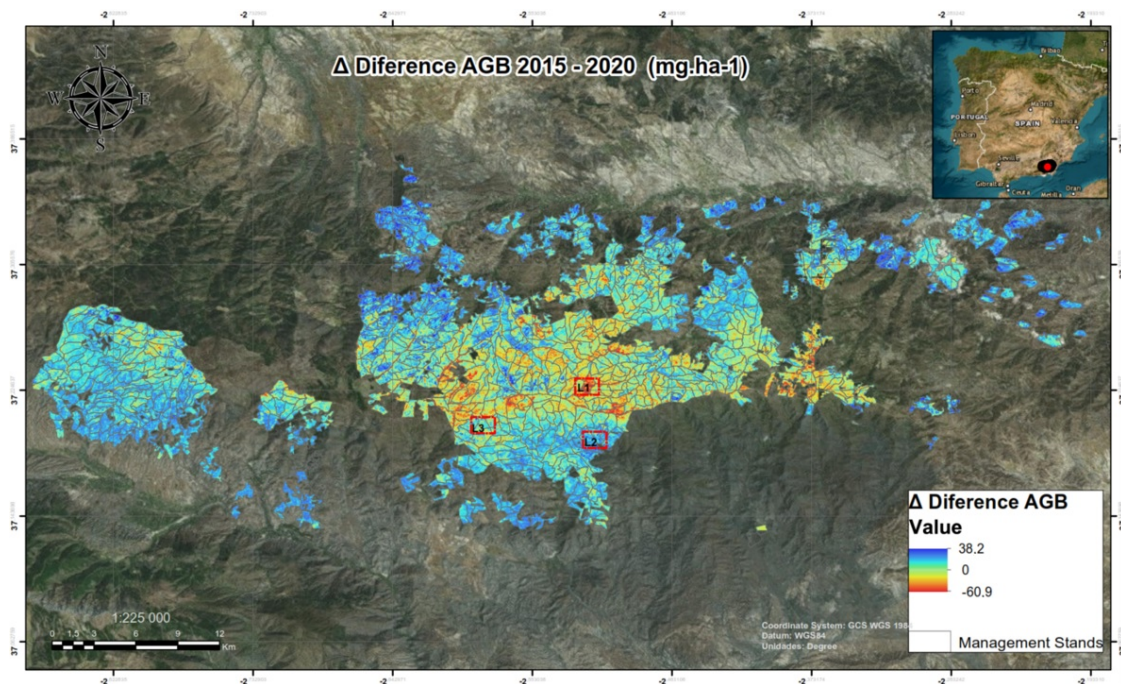


Figure 6. Aboveground biomass (AGB) changes between 2015–2021, assessed using ALOS PALSAR 2-Sentinel 1-Landsat 8 and textures in *Pinus* spp. plantations in Southern Spain.

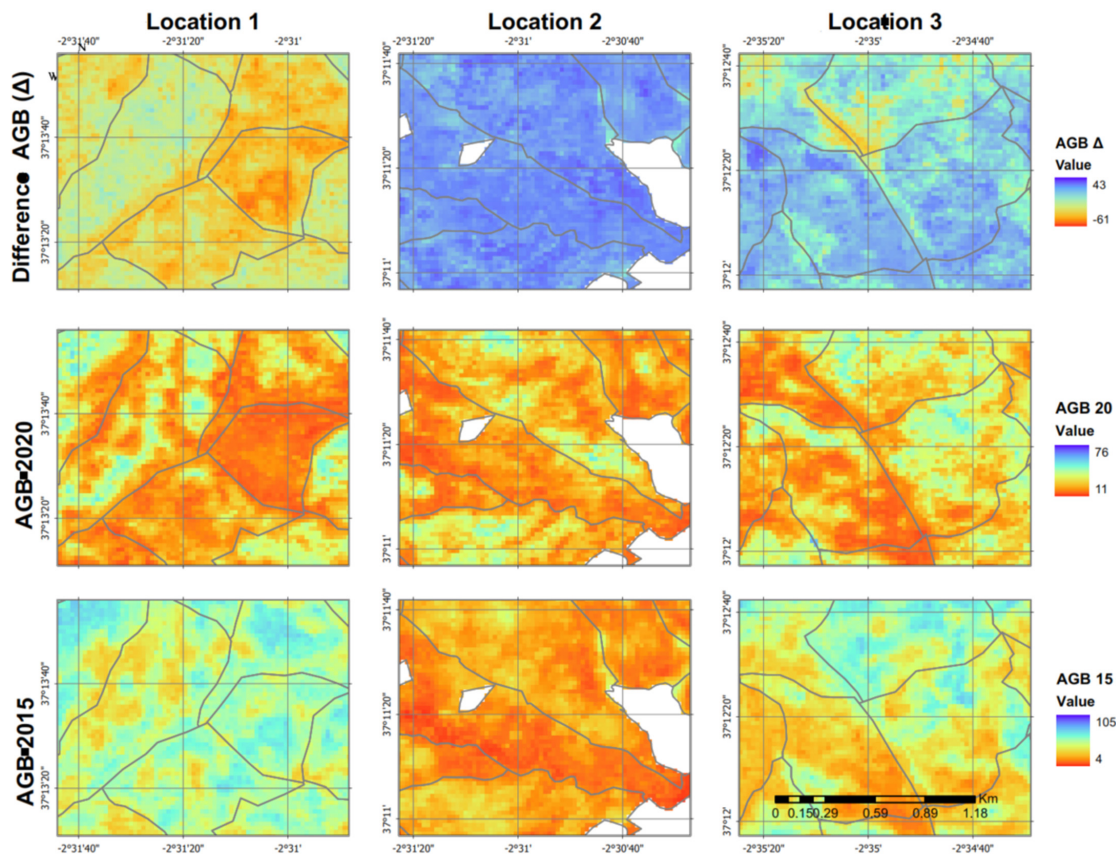


Figure 7. Example of a detailed pattern of aboveground (AGB) change between 2015–2021, assessed using ALOS PALSAR 2-Sentinel 1-Landsat 8 and textures in *Pinus* spp. plantations in Southern Spain.

4. Discussion

Biomass assessment in natural and planted forests with high biomass accumulation is a key source of uncertainty in forest management. Thus, in this study field, biomass measurements are contrasted with biomass extrapolated from different multispectral and SAR remote sensing data [11,13]. Previous studies have demonstrated the utility of open-access spaceborne data, such as Landsat, Sentinel-1, and ALOS-PALSAR data, for the production of maps of forest parameters [5,50,51]. This study represents a new contribution to these previous efforts. A processing framework with which to retrieve forest key parameters, integrating SAR L- and C-band, optical vegetation indices, and textural indices, was proposed for Mediterranean *Pinus* spp. plantations. The proposed methodology used open-source data and software for the image processing and machine learning algorithms to estimate temporal changes in AGB biomass. Also, the selected forest type (e.g., pine plantations) is one of the dominant types of land cover in large areas worldwide, and has important implications in wood production and conservation. Our results, which agree with prior studies, found that SAR-optical and multispectral earth observation data can be integrated to assess changes in key structural attributes of forests [7,52].

4.1. Forest Structural Variables

For forest management, height, dbh, and biomass are important variables which are closely linked to silvicultural interventions such as thinning and harvesting operations. Thus, accurate predictions of these forest parameters are needed. According to previous studies, ALS and SAR data provide the most accurate estimations of forest structural variables, with approximately 15–20% RMSE for AGB estimation and 5–10% RMSE for height [50,53,54]. In this study, four structural variables were estimated (e.g., density, dominant height, AGB, and dbh) based on global coverage, freely available optical and SAR data, and open-source software. The model performance obtained in this study (i.e., R^2 between 0.35–0.55; RMSE between 20–58% for 2015 and R^2 between 0.25–0.70; RMSE between 20–60% for 2020) were consistent with those of previous studies that have used similar methodological approaches for forest structural assessment [50,55,56] and mapping of AGB by combining Landsat-8 and ICESat-2 data ($R^2 = 0.58$) [57], but lower than others ($R^2 = 0.64$) [50,58]. However, our models did not improve with the inclusion of SAR data, since the performance of the combined ALOS 2-Sentinel-1-Landsat 8 model for 2015 ($R^2 = 0.55$, $RMSE = 19.88 \text{ Mg}\cdot\text{ha}^{-1}$) was not much superior to that of the Landsat 8 model ($R^2 = 0.52$, $RMSE = 20.54 \text{ Mg}\cdot\text{ha}^{-1}$). This is in accordance with some studies wherein the coefficient of determination did not increase considerably when combined with optical and SAR data [55,56,59]. This may be related to the reflected signals received by sensors [51]. On the other hand, in other types of ecosystems, better biomass estimation models have been obtained using SAR-HV polarization data [55] or photogrammetry and textural metrics from very high-resolution optical images (0.5–1 m) [60,61]. In our study, the radar variables that showed the best performance in AGB-Random Forest models were certain texture variables derived from the HV mode. Previous research has shown that HV polarization has a stronger correlation with AGB than HH polarization because HV is less affected by soil and vegetation moisture [62]. Additionally, topography has less impact on HV [63]. Differences may be also related to the spatial heterogeneity of forest stands [64], radar calibration, orthorectification, water saturation in mountain ecosystems [65], and field estimation errors propagating through the analysis of forest biomass [66]. According to the variables' importance rankings, Landsat 8 spectral and ALOS2/PALSAR2 L-band data played a significant role in predicting AGB. According to other studies that focus on mapping AGB and tree canopy height, near-infrared and shortwave regions are crucial to predicting AGB from multispectral image sources [66], demonstrating the usefulness of Landsat data in predicting AGB. In terms of the variables derived from the L-band, this study also supports the findings of Huang et al. [67], who demonstrated that texture features of the HV and HH polarizations influence AGB predictions more than the initial backscatter PALSAR data. However, SAR C-band polarization had little effect on the accuracy of the

Random Forest model with Sentinel-1 data. According to previous research comparing the efficacy of L- and C-band SAR data for AGB estimation, L-band data typically outperform C-band data due to their greater ability to penetrate the canopy [68]. On the other hand, SAR texture measurements may be better able to distinguish spatial information from noise in SAR data [19]. Additionally, backscatter behaves differently depending on the soil and vegetation moisture levels, as well as the topography of the surface, which increases the observed prediction errors [69]. Indeed, SAR backscatter is sensitive to humidity. For example, Ghaderpour et al. [3] describe how observational uncertainties due to atmospheric noise can be considered to define weights for measurements rather than eliminating them in machine learning models. Using SAR data collected during the dry summer season under comparable meteorological circumstances could reduce this effect. Finally, one last factor that must be considered is the process of selecting variables. As the work of Pham et al. [70] has highlighted, it is still challenging to identify the most critical features in a dataset, a process should be improved using machine learning models.

A saturation of the SAR signal was observed at a relatively low biomass of 60–70 mg/ha⁻¹, in concordance with previous studies [57]. Imhoff [57] reported the L-band saturation threshold to be 40 Mg ha⁻¹ in different forest ecosystems (broad-leaved—USA, pine forests—USA, and pine forests—France). This value was closer to that observed in Mediterranean pine plantations (70 Mg ha⁻¹) [71]. In contrast to more complex pine forests (e.g., boreal and hemi-boreal woods in Scandinavian countries [72]), the backscatter of Mediterranean pine forests appears to be more variable, which may be the result, considering that our assessments were made in a sparser forest [73].

4.2. Forest Applications

Open-access remote sensing can be used to upgrade key forest parameters (e.g., dominant height, diameter, and biomass) to support forest management plans. Forest biomass mapping from SAR and optic data showed a reasonable agreement when benchmarking with ALS-based AGB predictions. This was accomplished by combining multispectral imagery, SAR, and textural data. Limitations related to a mosaic of Mediterranean pine plantations were reflected in the moderate agreement between the Random Forest predictions and the multisensory-based model estimates of AGB ($R^2 = 0.50$). Despite these limitations, our approach has the potential to be relevant and helpful in the creation of more effective tools and methods based on hierarchical modeling techniques and remote sensing data using high-resolution temporal images (e.g., Landsat and SAR), which can be highly effective where limited ALS are available. Therefore, the synergistic use of optical (Landsat 8), ALOS2/PALSAR2 L-band, and Sentinel 1 SAR data to derive AGB over large areas lacking complete coverage of ALS data may be an accurate approach to tracking biomass changes.

The upcoming NASA-ISRO Synthetic Aperture Radar satellite mission in 2023 [74], which will deliver denser L-band time-series data at a higher spatial resolution (12 m), highlights the potential of integrating optical, LiDAR, and SAR data to assess temporal changes in biomass [75]. These methodologies provide a foundation for AGB estimations at different scales, and are especially relevant to countries or regions without field or ALS reference data. Since ALS-based AGB (and other key forest variables) observations are currently the most reliable reference data available for model fitting and the extrapolation of AGB dynamics, it is possible to apply species-specific AGB models derived from national or regional field surveys and integrated optical and SAR data. This is crucial for countries or regions that cannot afford to acquire fresh ALS or field data, as well as for temporal studies. Nevertheless, methods should be adapted to different forest types, especially in places where field and ALS reference data are unavailable. Sensor and vegetation characteristics have an impact on the accuracy of satellite-based AGB estimations [76].

5. Conclusions

Biomass estimation is a key variable for forest management due to its impact on the adaptation of forest systems to climate change. This variable is crucial for Mediterranean pine forests located on high-density plantations. The current work used optical (Landsat 8), ALOS2/PALSAR2 L-band, and Sentinel 1 SAR data to derive AGB in order to track biomass changes over large forest areas which lack ALS data. The study shows that models requiring fewer input parameters to estimate forest biomass are highly applicable and significant. Forest managers and forest agencies can use this methodology to upgrade AGB maps for applications in forests. The biomass models with the highest performance utilized ALS-ALOS2-Sentinel 1-Landsat 8 data. It is noteworthy that the individual Sentinel 1 and Landsat 8 models yielded similar results. Maps of the forest's structural variables were also generated to assess changes using the ALOS PALSAR 2-Sentinel 1-Landsat 8 model. Integrating open-access satellite optical and SAR data can significantly enhance AGB estimates for the purpose of consistent and long-term monitoring of forest carbon dynamics. Additionally, this research has the potential to be relevant to and helpful in the creation of more effective tools and methods based on open remote sensing data, providing better regional and global AGB information. The present approach can also be extended to the correlation of biomass with soil organic carbon to analyze the carbon sequestration potential of large pine plantations. Using this study as a foundation, deeper learning-based methods for the disentangled feature generation of SAR sensors and integrated modeling can be developed in the future.

Supplementary Materials: The following are available online at <https://www.mdpi.com/article/10.3390/rs15133430/s1>: Figure S1. Study area of *Pinus* spp. plantations in Sierra de los Filabres (Southern Spain) and location of sample plots. Figure S2. RGB visualization of the ALOS-PALSAR 2 data in the study area, R: HH, G: HV, B: NDBI. Figure S3. Pearson correlations for NDVI (Landsat 8) and HV (ALOS PALSAR 2) with basal area and biomass of *Pinus* spp. plantations in Sierra de los Filabres (Southern Spain). Figure S4. Recursive feature selection, outer resampling method. Figure S5. Variance importance ranking predictors in the best-fit random forest models for AGB Wt, basal area (BA), N trees per hectare, and diameter of the tree for 2015. Figure S6. Coefficients of the model validation test of the final models (ALOS PALSAR 2-SENTINEL1-LANDSAT8) for 2015; the red line shows the 1:1 line references and the blue line shows the random forest regression model. Figure S7. Basal Area (G) change between 2015 and 2020 using the ALOS PALSAR 2-Sentinel 1-Landsat 8 Random Forest model and textures of second order in *Pinus* spp. plantations in Southern Spain. Figure S8. Assman's dominant height (Ho) change between 2015 and 2020 using the ALOS PALSAR 2-Sentinel 1-Landsat 8 Random Forest model and textures of second order in *Pinus* spp. plantations in Southern Spain. Figure S9. Δ Mean square diameter (Dg) change between 2015 and 2020 using the ALOS PALSAR 2-Sentinel 1-Landsat 8 Random Forest model and textures of second order in *Pinus* spp. plantations in Southern Spain. Figure S10. Δ Difference number of trees (ha^{-1}) between 2015 and 2020 using the ALOS PALSAR 2-Sentinel 1-Landsat 8 Random Forest model and textures of second order in *Pinus* spp. plantations in Southern Spain. Figure S11. a. Map of AGB biomass 2015; b. map of AGB biomass 2020. Figure S12. a. Map of basal area 2015; b. map of basal area 2020. Figure S13. a. Map of mean square diameter (Dg) 2015; b. map of mean square diameter (Dg) 2020. Figure S14. Map of number of trees per Ha 2015; b. Map of number of trees per Ha 2020. Figure S15. Map of number of trees per Ha 2015; b. map of number of trees per Ha 2020. Table S1. Height and diameter equations used for inventory data update (Guzmán Álvarez et al., 2012). Diameter at breast height (D_i , cm), number of stems (N, trees ha^{-1}), height (H_i , m), Site Index (IS) competition index (IC_i) tree age (E_i), biomass fractions (stem W_s , thick branches W_{tkb} , medium branches W_{mb} , thin branches W_{tnb} , roots W_r , thick-medium branches W_{tkmb}).

Author Contributions: Conceptualization, R.M.N.-C., E.A.V.P. and M.A.V.M.; methodology, E.A.V.P., R.M.N.-C. and M.A.V.M.; formal analysis, E.A.V.P., M.A.V.M. and F.J.R.G.; investigation, E.A.V.P., R.M.N.-C. and M.A.V.M.; resources, R.M.N.-C.; data cleansing, E.A.V.P. and M.A.V.M.; writing—original draft preparation, R.M.N.-C. and E.A.V.P.; writing—review and editing, all authors; supervision, R.M.N.-C.; project administration, R.M.N.-C.; acquisition of funding, R.M.N.-C. All authors have read and agreed to the published version of the manuscript.

Funding: This research was funded by SILVADAPT.NET (RED2018-102719-T), EVIDENCE (Ref: 2822/2021) and REMEDIO (PID2021-128463OB-I00).

Data Availability Statement: The data presented in this study are available upon request from the corresponding author. The data are not publicly available due to institutional restrictions.

Acknowledgments: We would like to acknowledge the support provided by SILVADAPT.NET (RED2018-102719-T), EVIDENCE (Ref: 2822/2021) and REMEDIO (PID2021-128463OB-I00). We would also like to acknowledge the financial and institutional support of the University of Cordoba-Campus de Excelencia CEIA3. The authors acknowledge and thank the Mediterranean Forest Global Change Observatory for its support through the “Scientific Infrastructures for Global Change Monitoring and Adaptation in Andalusia (INDALO)—LIFEWATCH-2019-04-AMA-01” project, which was co-financed with FEDER funds corresponding to the Pluriregional Operational Programme of Spain 2014–2020. We are grateful to the “Consejería de Medioambiente y Ordenación del Territorio” (Junta de Andalucía) and the “RED SEDA NETWORK” (Junta de Andalucía), for providing field work and data support.

Conflicts of Interest: The authors declare no conflict of interest.

References

1. Novo-Fernández, A.; Barrio-Anta, M.; Recondo, C.; Cámara-Obregón, A.; López-Sánchez, C.A. Integration of national forest inventory and nationwide airborne laser scanning data to improve forest yield predictions in north-western Spain. *Remote Sens.* **2019**, *11*, 1693. [[CrossRef](#)]
2. Hartmann, H.; Bastos, A.; Das, A.J.; Esquivel-Muelbert, A.; Hammond, W.M.; Martínez-Vilalta, J.; Allen, C.D. Climate change risks to global forest health: Emergence of unexpected events of elevated tree mortality worldwide. *Annu. Rev. Plant Biol.* **2022**, *73*, 673–702. [[CrossRef](#)]
3. Ghaderpour, E.; Mazzanti, P.; Mugnozza, G.S.; Bozzano, F. Coherency and phase delay analyses between land cover and climate across Italy via the least-squares wavelet software. *Int. J. Appl. Earth Obs. Geoinf.* **2023**, *118*, 103241. [[CrossRef](#)]
4. Li, Y.; Li, M.; Wang, Y. Forest Aboveground Biomass Estimation and Response to Climate Change Based on Remote Sensing Data. *Sustainability* **2022**, *14*, 14222. [[CrossRef](#)]
5. Puliti, S.; Hauglin, M.; Breidenbach, J.; Montesano, P.; Neigh CS, R.; Rahlf, J.; Astrup, R. Modelling above-ground biomass stock over Norway using national forest inventory data with ArcticDEM and Sentinel-2 data. *Remote Sens. Environ.* **2020**, *236*, 111501. [[CrossRef](#)]
6. Lister, A.J.; Andersen, H.; Frescino, T.; Gatzolis, D.; Healey, S.; Heath, L.S.; Wilson, B.T. Use of remote sensing data to improve the efficiency of national forest inventories: A case study from the United States national forest inventory. *Forests* **2020**, *11*, 1364. [[CrossRef](#)]
7. Pardini, M.; Armston, J.; Qi, W.; Lee, S.K.; Tello, M.; Cazcarra Bes, V.; Fatoyinbo, L.E. Early lessons on combining lidar and multi-baseline SAR measurements for forest structure characterization. *Surv. Geophys.* **2019**, *40*, 803–837. [[CrossRef](#)]
8. Ellison, D.; Lundblad, M.; Petersson, H. Carbon accounting and the climate politics of forestry. *Environ. Sci. Policy* **2011**, *14*, 1062–1078. [[CrossRef](#)]
9. Englhart, S.; Keuck, V.; Siegert, F. Modeling aboveground biomass in tropical forests using multi-frequency SAR data—A comparison of methods. *IEEE J. Sel. Top. Appl. Earth Obs. Remote Sens.* **2012**, *5*, 298–306. [[CrossRef](#)]
10. le Toan, T.; Quegan, S.; Davidson, M.W.J.; Balzter, H.; Paillou, P.; Papathanassiou, K.; Plummer, S.; Rocca, F.; Saatchi, S.; Shugart, H.; et al. The BIOMASS mission: Mapping global forest biomass to better understand the terrestrial carbon cycle. *Remote Sens. Environ.* **2011**, *115*, 2850–2860. [[CrossRef](#)]
11. Lu, D. The potential and challenge of remote sensing-based biomass estimation. *Int. J. Remote Sens.* **2006**, *27*, 1297–1328. [[CrossRef](#)]
12. Hyde, P.; Dubayah, R.; Peterson, B.; Blair, J.B.; Hofton, M.; Hunsaker, C. Mapping forest structure for wildlife habitat analysis using waveform lidar: Validation of montane ecosystems. *Remote Sens. Environ.* **2005**, *96*, 427–437. [[CrossRef](#)]
13. Lu, D.; Chen, Q.; Wang, G.; Liu, L.; Li, G.; Moran, E. A survey of remote sensing-based aboveground biomass estimation methods in forest ecosystems. *Int. J. Digit. Earth* **2016**, *9*, 63–105. [[CrossRef](#)]
14. Vashum, K.T.; Jayakumar, S. Methods to estimate above-ground biomass and carbon stock in natural forests—A review. *J. Ecosyst. Ecography* **2012**, *2*, 4. [[CrossRef](#)]
15. Powell, S.L.; Cohen, W.B.; Healey, S.P.; Kennedy, R.E.; Moisen, G.G.; Pierce, K.B.; Ohmann, J.L. Quantification of live aboveground forest biomass dynamics with Landsat time-series and field inventory data: A comparison of empirical modeling approaches. *Remote Sens. Environ.* **2010**, *114*, 1053–1068. [[CrossRef](#)]
16. Andres-Mauricio, J.; Valdez-Lazalde, J.R.; George-Chacón, S.P.; Hernández-Stefanoni, J.L. Mapping structural attributes of tropical dry forests by combining Synthetic Aperture Radar and high-resolution satellite imagery data. *Appl. Veg. Sci.* **2021**, *24*, e12580. [[CrossRef](#)]
17. Alappat, V.O.; Joshi, A.K.; Krishnamurthy, Y.V. Tropical Dry Deciduous Forest Stand Variable Estimation Using SAR Data. *J. Indian Soc. Remote Sens.* **2011**, *39*, 583–589. [[CrossRef](#)]

18. Tian, X.; Su, Z.; Chen, E.; Li, Z.; van der Tol, C.; Guo, J.; He, Q. Estimation of forest above-ground biomass using multi-parameter remote sensing data over a cold and arid area. *Int. J. Appl. Earth Obs. Geoinf.* **2012**, *14*, 160–168.
19. Santi, E.; Paloscia, S.; Pettinato, S.; Fontanelli, G.; Mura, M.; Zolli, C.; Maselli, F.; Chiesi, M.; Bottai, L.; Chirici, G. The potential of multifrequency SAR images for estimating forest biomass in Mediterranean areas. *Remote Sens. Environ.* **2017**, *200*, 63–73. [[CrossRef](#)]
20. Luo, P.; Liao, J.; Shen, G. Combining spectral and texture features for estimating leaf area index and biomass of maize using sentinel-1/2, and landsat-8 data. *IEEE Access* **2020**, *8*, 53614–53626. [[CrossRef](#)]
21. Sarker, M.L.R.; Nichol, J.; Iz, H.B.; Ahmad, B.B.; Rahman, A.A. Forest biomass estimation using texture measurements of high-resolution dual-polarization C-band SAR data. *IEEE Trans. Geosci. Remote Sens.* **2013**, *51*, 3371–3384. [[CrossRef](#)]
22. Champion, I.; da Costa, J.-P.; Godineau, A.; Villard, L.; Dubois-Fernandez, P.; le Toan, T.; da Costa, J.P.; Dubois-Fernandez, P.; le Toan, T. Canopy structure effect on SAR image texture versus forest biomass relationships. *EARSeL Eproc.* **2013**, *12*, 25–32.
23. Hernández-Stefanoni, J.L.; Gallardo-Cruz, J.A.; Meave, J.A.; Rocchini, D.; Bello-Pineda, J.; López-Martínez, J.O. Modeling α - and β -diversity in a tropical forest from remotely sensed and spatial data. *Int. J. Appl. Earth Obs. Geoinf.* **2012**, *19*, 359–368. [[CrossRef](#)]
24. Esteban, J.; Fernández-Landa, A.; Tomé, J.L.; Gómez, C.; Marchamalo, M. Identification of Silvicultural Practices in Mediterranean Forests Integrating Landsat Time Series and a Single Coverage of ALS Data. *Remote Sens.* **2021**, *13*, 3611. [[CrossRef](#)]
25. Bruggisser, M.; Dorigo, W.; Dostálová, A.; Hollaus, M.; Navacchi, C.; Schlaffer, S.; Pfeifer, N. Potential of sentinel-1 c-band time series to derive structural parameters of temperate deciduous forests. *Remote Sens.* **2021**, *13*, 798. [[CrossRef](#)]
26. Periasamy, S. Significance of dual polarimetric synthetic aperture radar in biomass retrieval: An attempt on Sentinel-1. *Remote Sens. Environ.* **2018**, *217*, 537–549. [[CrossRef](#)]
27. Nizalapur, V.; Jha, C.S.; Madugundu, R. Estimation of above ground biomass in erkel tropical forested area using multi frequency DLR ESAR data. *Int. J. Geomat. Geosci.* **2010**, *1*, 167–178.
28. Forkuor, G.; Benewinde Zoungrana, J.B.; Dimobe, K.; Ouattara, B.; Vadrevu, K.P.; Tondoh, J.E. Above-ground biomass mapping in west erkele dryland forest using Sentinel-1 and 2 datasets—A case study. *Remote Sens. Environ.* **2020**, *236*, 111496. [[CrossRef](#)]
29. Potzschner, F.; Baumann, M.; Gasparri, N.I.; Conti, G.; Loto, D.; Piquer-Rodríguez, M.; Kuemmerle, T. Ecoregion-wide, multi-sensor biomass mapping highlights a major underestimation of dry forests carbon stocks. *Remote Sens. Environ.* **2022**, *269*, 112849. [[CrossRef](#)]
30. Nuthammachot, N.; Askar, A.; Stratoulas, D.; Wicaksono, P. Combined use of Sentinel-1 and Sentinel-2 data for improving above-ground biomass estimation. *Geocarto Int.* **2020**, *37*, 366–376. [[CrossRef](#)]
31. Morin, D.; Planells, M.; Guyon, D.; Villard, L.; Mermoz, S.; Bouvet, A.; Thevenon, H.; Dejoux, J.F.; Le Toan, T.; Dedieu, G. Estimation and mapping of forest structure parameters from open access satellite images: Development of a generic method with a study case on coniferous plantation. *Remote Sens.* **2019**, *11*, 1275. [[CrossRef](#)]
32. Chen, L.; Ren, C.; Zhang, B.; Wang, Z.; Xi, Y. Estimation of forest above-ground biomass by geographically weighted regression and machine learning with sentinel imagery. *Forests* **2018**, *9*, 582. [[CrossRef](#)]
33. Fernández Cancio, A.F.; Navarro Cerrillo, R.M.; Sánchez-Salguero, R.; Fernández, R.F.; Menéndez, E.M. Viabilidad fitoclimática de las repoblaciones de pino silvestre (*Pinus sylvestris* L.) en la Sierra de los Filabres (Almería). *Ecosistemas* **2011**, *20*, 124–144.
34. Navarrete-Poyatos, M.A.; Navarro-Cerrillo, R.M.; Lara-Gómez, M.A.; Duque-Lazo, J.; Varo, M.d.l.A.; Palacios Rodriguez, G. Assessment of the carbon stock in pine plantations in Southern Spain through ALS data and K-nearest neighbor algorithm-based models. *Geosciences* **2019**, *9*, 442. [[CrossRef](#)]
35. MITECO. Tercer Inventario Forestal Nacional (IFN3). 2007. Available online: <https://www.miteco.gob.es/es/biodiversidad/servicios/banco-datos-naturaleza/informacion-disponible/ifn3.aspx> (accessed on 20 July 2022).
36. Guzmán Álvarez, J.R.; Venegas Troncoso, J.; Seseña Rengel, A.; Sillero Almazán, M.L.; Rodríguez Álvarez, J.A. *Biomasa Forestal en Andalucía. 1. Modelo de Existencias, Crecimiento y Producción*; Ediciones Mundi-Prensa: Madrid, Spain, 2008.
37. Ruiz-Peinado, R.; del Rio, M.; Montero, G. New models for estimating the carbon sink capacity of Spanish softwood species. *For. Syst.* **2011**, *20*, 176–188. [[CrossRef](#)]
38. Almeida-Filho, R.; Shimabukuro, Y.E.; Rosenqvist, A.; Sánchez, G.A. Using dual-polarized ALOS PALSAR data for detecting new fronts of deforestation in the Brazilian Amazônia. *Int. J. Remote Sens.* **2009**, *30*, 3735–3743. [[CrossRef](#)]
39. Dong, L.; Du, H.; Han, N.; Li, X.; Zhu, D.; Mao, F.; Zhang, M.; Zheng, J.; Liu, H.; Huang, Z.; et al. Application of Convolutional Neural Network on Lei Bamboo Above-Ground-Biomass (AGB) Estimation Using Worldview-2. *Remote Sens.* **2020**, *12*, 958. [[CrossRef](#)]
40. Zvoleff, A. Package ‘glcm’, version 1.6.1. Available online: <http://cran.uni-muenster.de/web/packages/glcm/glcm.pdf> (accessed on 21 January 2022).
41. Haralick, R.M.; Dinstein, I.; Shanmugam, K. Textural Features for Image Classification. *IEEE Trans. Syst. Man Cybern.* **1973**, *SMC-3*, 610–621. [[CrossRef](#)]
42. McGaughey, R.J. *FUSION/LDV: Software for LIDAR Data Analysis and Visualization*; USDA Forest Service. PNW: Vancouver, WA, USA, 2007.
43. Isenburg, M. *LAStools*; Rapidlasso GmbH: Gilching, Germany, 2017.
44. Liaw, A.; Wiener, M. Classification and Regression by Random Forest. 2002. Available online: <http://www.stat.berkeley.edu/> (accessed on 21 January 2022).

45. Miranda, E.N.; Barbosa, B.H.G.; Silva, S.H.G.; Monti, C.A.U.; Tng, D.Y.P.; Gomide, L.R. Variable selection for estimating individual tree height using genetic algorithm and random forest. *Forest Ecol. Manag.* **2022**, *504*, 119828. [[CrossRef](#)]
46. Hastie, T.; Tibshirani, R.; Friedman, J. Model Assessment and Selection. In *The Elements of Statistical Learning*; Springer Series in Statistics; Springer: New York, NY, USA, 2008; pp. 219–259.
47. Kuhn, M.; Wing, J.; Weston, S.; Williams, A.; Keefer, C.; Engelhardt, A.; Cooper, T.C.; Mayer, Z.; Kenkel, B.; Benesty, M.; et al. Package ‘Caret’—Classification and Regression Training version 6.0-93. 2022. Available online: <https://cran.r-project.org/web/packages/caret/caret.pdf> (accessed on 12 February 2022).
48. Crookston, N.L.; Finley, A.O. yaImpute: AR Package for Nearest Neighbor Imputation Routines, Variance Estimation, and Mapping. Available online: <http://cran.r-project.org> (accessed on 10 February 2022).
49. R Development Core Team. R: A Language and Environment for Statistical Computing. Available online: <https://www.R-project.org/> (accessed on 14 January 2022).
50. Guerra-Hernández, J.; Narine, L.L.; Pascual, A.; Gonzalez-Ferreiro, E.; Botequim, B.; Malambo, L.; Godinho, S. Aboveground biomass mapping by integrating ICESat-2, SENTINEL-1, SENTINEL-2, ALOS2/PALSAR2, and topographic information in Mediterranean forests. *Gisci. Remote Sens.* **2022**, *59*, 1509–1533. [[CrossRef](#)]
51. Silveira, E.M.; Radeloff, V.C.; Martinuzzi, S.; Pastur, G.J.M.; Bono, J.; Politi, N.; Pidgeon, A.M. Nationwide native forest structure maps for Argentina based on forest inventory data, SAR Sentinel-1 and vegetation metrics from Sentinel-2 imagery. *Remote Sens. Environ.* **2023**, *285*, 113391. [[CrossRef](#)]
52. Quegan, S.; Le Toan, T.; Chave, J.; Dall, J.; Exbrayat, J.F.; Minh, D.H.T.; Williams, M. The European Space Agency BIOMASS mission: Measuring Forest above-ground biomass from space. *Remote Sens. Environ.* **2019**, *227*, 44–60. [[CrossRef](#)]
53. Yu, X.; Hyypä, J.; Karjalainen, M.; Nurminen, K.; Karila, K.; Vastaranta, M.; Katoh, M. Comparison of laser and stereo optical, SAR and InSAR point clouds from air-and space-borne sources in the retrieval of forest inventory attributes. *Remote Sens.* **2015**, *7*, 15933–15954. [[CrossRef](#)]
54. Martin, Q.; White, J.C.; Coops, N.C. Comparing Airborne and Spaceborne Photon-Counting LiDAR Canopy Structural Estimates across Different Boreal Forest Types. *Remote Sens. Environ.* **2021**, *262*, 112510.
55. Li, Y.; Li, M.; Li, C.; Liu, Z. Forest aboveground biomass estimation using Landsat 8 and Sentinel-1A data with machine learning algorithms. *Sci. Rep.* **2020**, *10*, 9952. [[CrossRef](#)]
56. Zhang, W.; Zhao, L.; Li, Y.; Shi, J.; Yan, M.; Ji, Y. Forest Above-Ground Biomass Inversion Using Optical and SAR Images Based on a Multi-Step Feature Optimized Inversion Model. *Remote Sens.* **2022**, *14*, 1608. [[CrossRef](#)]
57. Imhoff, M.L. Radar backscatter and biomass saturation: Ramifications for global biomass inventory. *IEEE Trans. Geosci. Remote Sens.* **1995**, *33*, 511–518. [[CrossRef](#)]
58. Nesha, M.K.; Hussin, Y.A.; van Leeuwen, L.M.; Sulistioadi, Y.B. Modeling and mapping aboveground biomass of the restored mangroves using ALOS-2 PALSAR-2 in East Kalimantan, Indonesia. *Int. J. Appl. Earth Obs. Geoinf.* **2020**, *91*, 102158. [[CrossRef](#)]
59. Kumar, L.; Mutanga, O. Remote Sensing of Above-Ground Biomass. *Remote Sens.* **2017**, *9*, 935. [[CrossRef](#)]
60. Kuplich, T.M.; Salvatori, V.; Curran, P.J. JERS-1/SAR backscatter and its relationship with biomass of regenerating forests. *Int. J. Remote Sens.* **2000**, *21*, 2513–2518. [[CrossRef](#)]
61. Dube, T.; Mutanga, O. Investigating the robustness of the new Landsat-8 Operational Land Imager derived texture metrics in estimating plantation forest aboveground biomass in resource constrained areas. *ISPRS J. Photogramm. Remote Sens.* **2015**, *108*, 12–32. [[CrossRef](#)]
62. Pearse, G.D.; Dash, J.P.; Persson, H.J.; Watt, M.S. Comparison of high-density LiDAR and satellite photogrammetry for forest inventory. *ISPRS J. Photogramm. Remote Sens.* **2018**, *142*, 257–267. [[CrossRef](#)]
63. Williams, M.L.; Mitchell, A.L.; Milne, A.K.; Danaher, T.; Horn, G. Addressing critical influences on L-band radar backscatter for improved estimates of basal area and change. *Remote Sens. Environ.* **2020**, *272*, 112933. [[CrossRef](#)]
64. Sandberg, G.; Ulander, L.M.; Fransson, J.E.; Holmgren, J.; Le Toan, T. L- and P-band backscatter intensity for biomass retrieval in hemiboreal forest. *Remote Sens. Environ.* **2011**, *115*, 2874–2886. [[CrossRef](#)]
65. van Zyl, J.J. The Effect of Topography on Radar Scattering from Vegetated Areas. *IEEE Trans. Geosci. Remote Sens.* **1993**, *31*, 153–160. [[CrossRef](#)]
66. Réjou-Méchain, M.; Barbier, N.; Coutron, P.; Ploton, P.; Vincent, G.; Herold, M.; Pélissier, R. Upscaling Forest biomass from field to satellite measurements: Sources of errors and ways to reduce them. *Surv. Geophys.* **2019**, *40*, 881–911. [[CrossRef](#)]
67. Huang, H.; Liu, C.; Wang, X.; Zhou, X.; Gong, P. Integration of multi-resource remotely sensed data and allometric models for forest aboveground biomass estimation in China. *Remote Sens. Environ.* **2019**, *221*, 225–234. [[CrossRef](#)]
68. Laurin, G.V.; Balling, J.; Corona, P.; Mattioli, W.; Papale, D.; Puletti, N.; Urban, M. Above-ground biomass prediction by Sentinel-1 multitemporal data in central Italy with integration of ALOS2 and Sentinel-2 data. *J. Appl. Remote Sens.* **2018**, *12*, 016008. [[CrossRef](#)]
69. Tanase, M.A.; Santoro, M.; De La Riva, J.; Fernando, P.; Le Toan, T. Sensitivity of X-, C-, and L-band SAR backscatter to burn severity in Mediterranean pine forests. *IEEE Trans. Geosci. Remote Sens.* **2010**, *48*, 3663–3675. [[CrossRef](#)]
70. Pham, H.T.; Awange, J.; Kuhn, M. Evaluation of Three Feature Dimension Reduction Techniques for Machine Learning-Based Crop Yield Prediction Models. *Sensors* **2022**, *22*, 6609. [[CrossRef](#)]

71. Montero, G.; Ruiz-Peinado, R.; Muñoz, M. *Producción de Biomasa y Fijación de CO₂ por los Bosques Españoles*; Serie Forestal 13; Instituto Nacional de Investigación y Tecnología Agraria y Alimentaria, Ministerio de Educación y Ciencia: Madrid, Spain, 2005; 270p.
72. Santoro, M.; Cartus, O.; Carvalhais, N.; Rozendaal, D.; Avitabile, V.; Araza, A.; Willcock, S. The global forest above-ground biomass pool for 2010 estimated from high-resolution satellite observations. *Earth Syst. Sci. Data* **2021**, *13*, 3927–3950. [[CrossRef](#)]
73. Narine, L.L.; Popescu, S.C.; Malambo, L. Using ICESat-2 to estimate and map forest aboveground biomass: A first example. *Remote Sens.* **2020**, *12*, 1824. [[CrossRef](#)]
74. Kumar, S. Polarimetric Distortion Analysis of L-and S-Band Airborne SAR (LS-ASAR): A Precursor Study of the Spaceborne Dual-Frequency L-and S-Band NASA ISRO Synthetic Aperture Radar (NISAR) Mission. *Eng. Proc.* **2022**, *27*, 77.
75. Khati, U.; Lavalle, M.; Singh, G. The role of time-series L-band SAR and GEDI in mapping sub-tropical above-ground biomass. *Front. Earth Sci.* **2021**, *9*, 752254. [[CrossRef](#)]
76. Araza, A.; De Bruin, S.; Herold, M.; Quegan, S.; Labriere, N.; Rodriguez-Veiga, P.; Avitabile, V.; Santoro, M.; Mitchard, E.T.A.; Ryan, C.M.; et al. A Comprehensive Framework for Assessing the Accuracy and Uncertainty of Global Above-Ground Biomass Maps. *Remote Sens. Environ.* **2022**, *272*, 112917. [[CrossRef](#)]

Disclaimer/Publisher's Note: The statements, opinions and data contained in all publications are solely those of the individual author(s) and contributor(s) and not of MDPI and/or the editor(s). MDPI and/or the editor(s) disclaim responsibility for any injury to people or property resulting from any ideas, methods, instructions or products referred to in the content.